Far-Field Drag Decomposition Applied to the Drag Prediction Workshop 5 Cases

Martin Gariépy,* Benoit Malouin,† Jean-Yves Trépanier,‡ and Éric Laurendeau§
École Polytechnique de Montréal, Montréal, Québec H3C 1K3, Canada

DOI: 10.2514/1.C032204

A far-field drag prediction and decomposition method has been applied to the results of the AIAA Drag Prediction Workshop 5 held in Louisiana during the summer of 2012. The method has two principal advantages: it allows the removal of spurious drag inherent to computational fluid dynamics solutions, and it allows the decomposition of drag into viscous, wave, and induced physical drag components. This research shows that accurate drag coefficients can be predicted on coarse grids when the spurious drag is extracted with the far-field method and that these results are closer to experimental values than drag coefficients computed on finer meshes when spurious drag is not extracted. The research also investigated the reasons behind the lift and drag losses found by some participants in the workshop. It is shown that the lift loss is caused by the boundary-layer separation at the wing root, inducing a reduction of 20% of the shock wave drag and a significant change in the wing loading. The initiation of buffet is also analyzed. The study shows that mesh refinement is critical to capture the physical effects of the flow, such as its separation, and provides an explanation of the discrepancies in results observed at the Drag Prediction Workshop 5.

Nomenclature

a	=	speed of sound, m/s
C_d	=	drag coefficient
C_l	=	lift coefficient
C_m	=	moment coefficient
C_p	=	pressure coefficient
D	=	drag, N
H	=	total enthalpy, J/kg
h	=	scale parameter
M	=	Mach number
$\boldsymbol{n}$	=	unit normal vector (n_x, n_y, n_z)
P	=	pressure, kPa
R	=	gas constant, J(kg · K)
S	=	relative to a surface, m^2
s	=	entropy, J/K
S_T	=	Trefftz plane
T	=	temperature, K or °C
$\boldsymbol{v}$	=	velocity vector (u, v, w), m/s
γ	=	specific heat ratio
ΔH	=	variation of total enthalpy relative to freestream, J/kg
Δs	=	variation of entropy relative to freestream, J/K
μ	=	viscosity, N · s/m^2
ρ	=	density, kg/m^3
τ	=	deviatoric stress tensor $(\boldsymbol{\tau}_x, \boldsymbol{\tau}_y, \boldsymbol{\tau}_z)$, N/m^2
Ω	=	volume, m^3

Subscripts

cut	=	symmetrical plane
ff	=	relative to far-field approach
i	=	relative to induced drag
irr	=	relative to irreversible drag
l	=	relative to laminar flow
nf	=	relative to near-field approach
sp	=	relative to spurious drag
t	=	relative to turbulent flow
v	=	relative to viscous drag
vw	=	relative to viscous and wave drag
w	=	relative to wave drag
∞	=	relative to freestream

I. Introduction

IN THE current economic environment, in which the price of oil skyrocketed to a historic high of more than $100 per barrel[¶] and the cost of fuel for an aircraft represents more than 20% of the operational cost of an airliner,[**] the aeronautical industry is trying to ensure that novel aircraft designs are fuel efficient. The identification and quantification of drag is of paramount importance in this endeavor, with the industry increasingly relying on computational fluid dynamics (CFD) analysis to perform drag analysis. According to industry criteria [1], accuracy in the computational fluid dynamics process should allow the prediction of drag coefficients within one drag count, which is equivalent to one ten-thousandth of the drag coefficient. Many studies have shown the impact of one drag count on the efficiency and performance of an aircraft. For example, Meredith [2] showed that one drag count is equivalent to a payload of 91 kg for a long-haul aircraft. It is for these reasons that NASA, sponsored by the Applied Aerodynamics Technical Committee, has set up the Drag Prediction Workshop (DPW) series, the primary objective of which is to assess the state of the art in numerical methods as tools for predicting aerodynamic coefficients.[††]

Based on converged CFD results, the traditional approach computes drag by integrating the pressure and friction forces acting on the aircraft configuration. This method is commonly called the

Presented as Paper 2013-2507 at the 31st AIAA Applied Aerodynamics Conference, San Diego, CA, 24–27 June 2013; received 19 November 2012; revision received 1 March 2013; accepted for publication 15 March 2013; published online 9 September 2013.

*Research Associate, Department of Mechanical Engineering; martin.gariepy@polymtl.ca. Member AIAA.

†Ph.D. Student, Department of Mechanical Engineering; benoit.malouin@polymtl.ca. Student Member AIAA.

‡Professor, Department of Mechanical Engineering; jean-yves.trepanier@polymtl.ca. Member AIAA.

§Assistant Professor, Department of Mechanical Engineering; eric.laurendeau@polymtl.ca. Member AIAA.

¶Data available online at http://en.wikipedia.org/wiki/Price_of_petroleum [retrieved 15 May 2013].

**Data available online at http://www.iata.org/whatwedo/workgroups/Documents/aoctf-FY0809-form41-report.pdf [retrieved 15 May 2013].

††Data available online at http://aaac.larc.nasa.gov/tsab/cfdlarc/aiaa-dpw/ [retrieved January 2012].

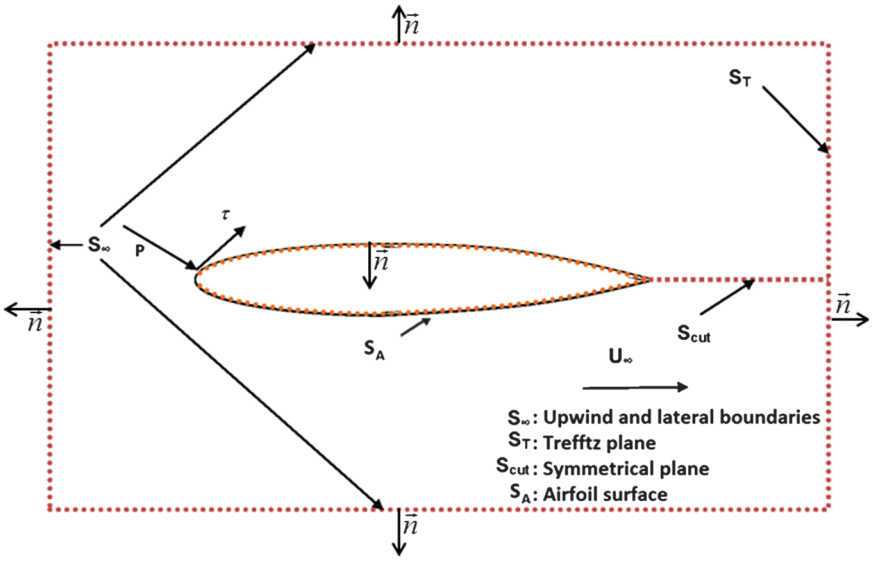

Fig. 1 Fixed control volume.

near-field method. Another technique, based on the linear momentum relation, has been developed by Van der Vooren and Destarac [3] based on the pioneering work of Van der Vooren and Slooff [4]. This technique, commonly called the far-field method, is a valuable and powerful tool for the aerodynamics engineer because it allows the physical decomposition of drag into wave drag, viscous drag, induced drag, and spurious drag, the latter being caused by numerical and truncation errors inherent to CFD computations. The far-field method allows engineers to physically and visually identify the sources of drag and, perhaps more importantly, to significantly increase drag coefficient accuracy by identifying and removing spurious drag. It is shown here that the computed drag coefficient obtained after removal of the spurious drag is much more mesh insensitive than it is without removal. The added benefit is the decrease in CPU time required to achieve mesh-independent accuracy [5].

In this article, the far-field drag prediction and decomposition method is applied to the test cases of the Drag Prediction Workshop 5 (DPW-5)[††] held in Louisiana during the summer of 2012. First, the far-field method is used to extract the spurious drag from the grid convergence study test case. Also, the far-field method is used to explain the physical reason for the lift and drag losses captured during the buffet study. It is shown that this lift loss is caused by boundary-layer separation at the wing root, which causes the loss of 20% of the shock wave. This loss results in a significant change in wing loading, which initiates buffet. A grid study shows that mesh refinement is critical to capture the boundary-layer separation and the corresponding lift and drag losses. It is also shown that the mesh provided by the DPW committee is not refined enough to capture the boundary-layer separation. This realization provides insights for the discrepancies in the team results. Finally, it is shown that the use of the far-field method to extract spurious drag leads to accurate drag prediction, along with increased agreement with the experimental results.

II. Theoretical Development

The far-field method is based on the linear momentum relation for a fixed control volume. The following résumé is mainly based on the theory of Van der Vooren and Destarac [3], who developed the original method, and on the works of Laurendeau and Boudreau [6], Gariépy et al. [5], and Gariépy and Trépanier [7], who proposed modifications to the original method.

Based on the linear momentum equation for an immersed body in a flow stream, as sketched in Fig. 1, the drag can be computed as follows:

$$D = \int_{S_T+S_\infty} -((p-p_\infty)n_x + \rho(u-u_\infty)(\boldsymbol{v}\cdot\boldsymbol{n}) - (\boldsymbol{\tau}_x\cdot\boldsymbol{n}))\,\mathrm{d}S \tag{1}$$

This drag can be called far-field drag, as it involves integration over control surfaces within the flowfield and not only at the fluid/solid boundary. However, in this form, the far-field drag cannot be broken down into simpler forms without some manipulations being performed first. Note that the physical breakdown of drag is based on thermodynamic processes, and its main goal [3] is to separate the drag generated by irreversible processes (shock waves and viscous effects) from the drag generated by reversible processes (wake vortices). The first step is to decompose the axial velocity defect, i.e., $u-u_\infty$, into two parts: one caused by reversible processes, Δu_*, and the other caused by irreversible processes, $\Delta\bar{u}$. Using thermodynamic relations and some assumptions, Gariépy and Trépanier [7] showed that the axial velocity defect caused by irreversible processes can be computed as follows:

$$\Delta\bar{u} = u - u_\infty\sqrt{1+\frac{2\Delta H}{u_\infty^2}-\frac{2}{M_\infty^2(\gamma-1)}\left[\left(\frac{p}{p_\infty}\right)^{\gamma-1/\gamma}-1\right]-\frac{v^2+w^2}{u_\infty^2}} \tag{2}$$

The latter equation is a variant of the original equation of Méheut and Bailly [8,9], which assumes negligible enthalpy variation. It can be shown [8] that the radical of the square root in the latter equation is always greater than or equal to zero, which allows the axial velocity defect to be a continuous function within the computational domain. This formulation is the major difference between the original far-field method of Van der Vooren and Destarac [3] and the version presented here.

It is useful to introduce the notation of Van der Vooren and Destarac [3]:

$$\boldsymbol{f} = -(p-p_\infty)\boldsymbol{n}_x - \rho\boldsymbol{u}(u-u_\infty) + \boldsymbol{\tau}_x \tag{3}$$

Assuming a flow without induced drag,[‡‡] the irreversible drag can be computed as follows:

$$D_{\mathrm{irr}} = \int_{S_T\cup S_\infty\cup S_a} (\boldsymbol{f}_{\mathrm{vw}}\cdot\boldsymbol{n})\,\mathrm{d}S \tag{4}$$

where the vector $\boldsymbol{f}_{\mathrm{vw}}$ is defined as follows:

$$\boldsymbol{f}_{\mathrm{vw}} = -(\rho\Delta\bar{u})\boldsymbol{u} \tag{5}$$

[‡‡]I.e., a two-dimensional flow or a flow with no lift.

Equation (4) can now be transformed into a volume integral using the Ostrogradsky theorem:

$$D_{\text{irr}} = \int_{S_T \cup S_\infty \cup S_a} (\boldsymbol{f}_{\text{vw}} \cdot \boldsymbol{n})\, \mathrm{d}S = \int_{\Omega} (\nabla \cdot \boldsymbol{f}_{\text{vw}})\, \mathrm{d}V \tag{6}$$

Note that, even if there is the presence of a shock wave, the Ostrogradsky theorem can be numerically applied because the shock wave can be excluded from the integration volume, hence leading $\boldsymbol{f}_{vw}$ to be a continuous over the computational domain.

A simple analysis of Eq. (2) shows that the axial velocity defect caused by irreversible processes is zero when the flow is isentropic. This makes it possible to restrict the integration of Eq. (6) to the nonisentropic zones of the flow. In the case of aerodynamic configurations such as an airfoil or a complete aircraft, the nonisentropic zones are the boundary layer, the viscous wake, and the near field zone of a shock wave in the case of transonic flows. The viscous and wave drag can then be defined by integrating Eq. (6) in these zones as follows:

$$D_v = \int_{\Omega_v} (\nabla \cdot \boldsymbol{f}_{\text{vw}})\, \mathrm{d}V \tag{7}$$

$$D_w = \int_{\Omega_w} (\nabla \cdot \boldsymbol{f}_{\text{vw}})\, \mathrm{d}V \tag{8}$$

The spurious drag is caused by spurious entropy, which in turn is caused by numerical and truncation errors, and by the addition of artificial dissipation [10]. The spurious drag is associated with irreversible drag, owing its contribution to entropy. Typically, strong pressure gradients are located at the nose of the fuselage and at the leading edge of the wings and stabilizers. An example of spurious drag is shown in Fig. 2. Ideally, these zones can be assumed to be isentropic, and the integration of Eq. (6) over them should be zero. Hence, spurious drag can be computed as follows:

$$D_{\text{sp}} = \int_{\Omega_{\text{sp}}} (\nabla \cdot \boldsymbol{f}_{\text{vw}})\, \mathrm{d}V \tag{9}$$

where the spurious volume is given by $\Omega_{\text{sp}} = \Omega \setminus (\Omega_v \cup \Omega_w)$. By definition, the vector $\boldsymbol{f}_{\text{vw}}$, i.e., Eq. (5), represents the forces acting on the control surface caused by the irreversible processes. The vector $\boldsymbol{f}_* = \boldsymbol{f} - \boldsymbol{f}_{\text{vw}}$ must then represent the force acting on the control surface caused by a reversible process. Van der Vooren and Destarac [3] showed that induced drag, which is caused by the difference in pressure between intrados and extrados (reversible process), can then be computed as follows:

$$D_i = \int_{\Omega_i} (\nabla \cdot \boldsymbol{f}_*)\, \mathrm{d}V + D_{\text{nf}} \tag{10}$$

To detect the various integration volumes, a number of different sensors can be used. The shock volume Ω_v can be detected by the Lovely and Haimes sensor [11]:

$$F_{\text{shock}} = \frac{\boldsymbol{v} \cdot \nabla p}{a|\nabla p|} \tag{11}$$

This sensor flags a cell whenever its numerical value is greater than or equal to one. Numerically, this volume must be expanded owing to nonphysical phenomena (such as entropy creation/destruction) occurring in the vicinity of the shock. The algorithm used in this work automatically selects the three closest neighbors of each initially flagged cell. An example of such a volume is shown in Fig. 3.

For a fully turbulent flow, the sensor of Tognaccini [12] is used to detect the viscous wake and boundary-layer volume Ω_v:

$$F_{\text{viscous}} = \frac{\mu_l + \mu_t}{\mu_l} \tag{12}$$

This sensor is activated whenever its numerical value is greater than or equal to 1.1 times the freestream value. An example of such a volume is shown in Fig. 4.

Theoretically, the induced drag volume could be as big as the computational domain. However, Esquieu [10] showed that induced drag suffers from nonphysical viscous dissipation in the far field due to the coarsening of the mesh. Accordingly, the induced drag volume Ω_i, following an original idea of Laurendeau and Boudreau [6], is constructed by selecting all the cells located at some distance from the configuration. An example of such volume is shown in Fig. 5.

Numerically, Tognaccini [12] has proposed reapplying the Ostrogradsky theorem on Eqs. (7–9) to handle a cell-by-cell surface

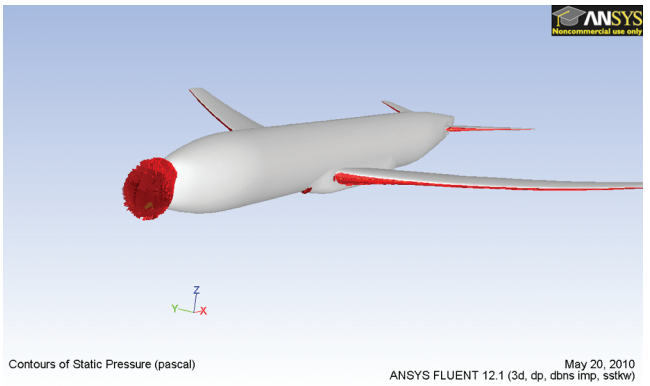

Fig. 2 Spurious volume for the DLR F6 at $Ma = 0.85$ and $C_L = 0.5$.

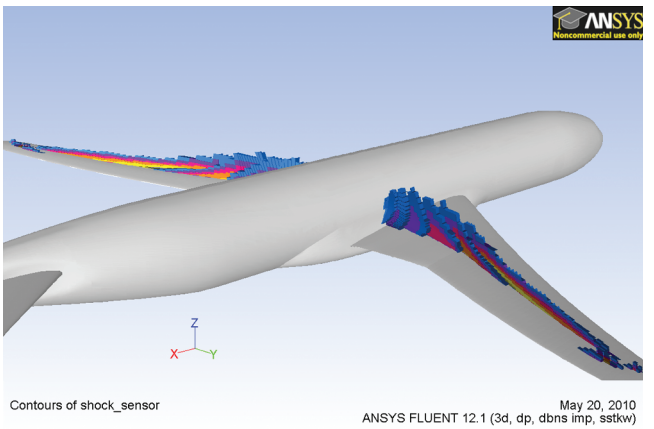

Fig. 3 Shock volume for the DLR F6 at $Ma = 0.85$ and $C_L = 0.5$.

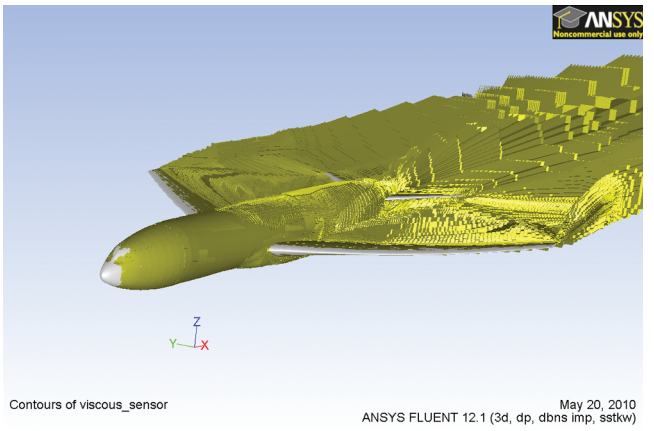

Fig. 4 Viscous volume for the DLR F6 at $Ma = 0.85$ and $C_L = 0.5$.

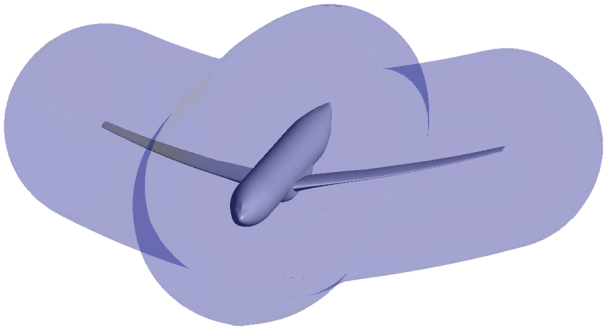

Fig. 5 Induced drag volume.

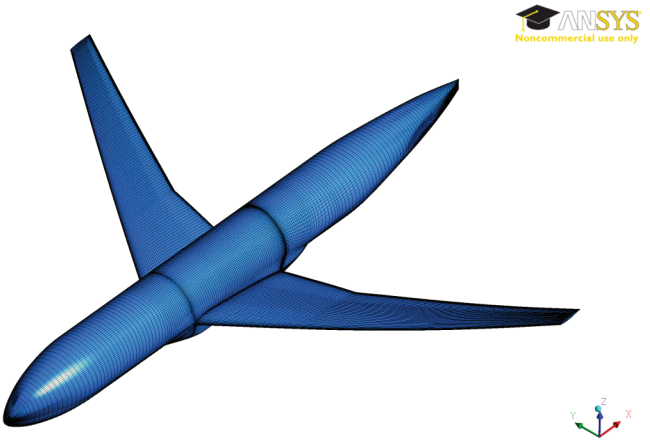

Fig. 6 Common Research Model.

flux integral, rather than a volume integral, because the flux values are a known quantity at the faces of these cells when a finite volume solver is used. For example, viscous drag can be computed as follows:

$$D_v = \sum_{i=1}^{N}\left(\sum_{j=1}^{k}\int_{S_{v(i,j)}} (\boldsymbol{f}_{\mathrm{vw}}\cdot\boldsymbol{n})\,\mathrm{d}S\right) \tag{13}$$

where N represents the number of cells in the viscous zone, k represents the number of faces of each cell, and $S_{v(i,j)}$ represents the jth face of the ith viscous cell.

In summary, the far-field drag D_{ff} can be decomposed and computed as follows:

$$\begin{aligned} D_{\mathrm{ff}} &= D_v + D_w + D_i + D_{\mathrm{sp}} \\ &= \int_{\Omega_v} (\nabla\cdot\boldsymbol{f}_{\mathrm{vw}})\,\mathrm{d}V + \int_{\Omega_w} (\nabla\cdot\boldsymbol{f}_{\mathrm{vw}})\,\mathrm{d}V \\ &\quad + \int_{\Omega_{\mathrm{sp}}} (\nabla\cdot\boldsymbol{f}_{\mathrm{vw}})\,\mathrm{d}V + \int_{\Omega_i} (\nabla\cdot\boldsymbol{f}_{*})\,\mathrm{d}V + D_{\mathrm{nf}} \end{aligned} \tag{14}$$

The net drag D_ϕ is the far-field drag in which the spurious drag has been removed:

$$D_\phi = D_{\mathrm{ff}} - D_{\mathrm{sp}} = \int_{\Omega_{v+w}} (\nabla\cdot\boldsymbol{f}_{\mathrm{vw}})\,\mathrm{d}V + \int_{\Omega_i} (\nabla\cdot\boldsymbol{f}_{*})\,\mathrm{d}V + D_{\mathrm{nf}} \tag{15}$$

Note that, in all the results presented from now on, it is the drag coefficient C_d rather than the drag itself that is computed:

$$C_d = \frac{D}{0.5\rho_\infty U_\infty^2 S} \tag{16}$$

where S represents the reference area.

III. Grids, Algorithms, and Geometry

All CFD computations are performed on the Common Research Model (CRM), a wing body with no tail.[§§] Information about this geometry can be found in Vassberg et al. [13], and this geometry is presented in Fig. 6. In this research, two sets of four grids are used.

The first set of grids was supplied by the organizing committee.[¶¶] It consists of four hybrid unstructured meshes with an O-O topology converted from multiblock grids, in which each edge has been divided by two during the refinement sequence. The tiny, coarse, medium, and fine grids have 1.3, 4.3, 10.2, and 34.5 million cells, respectively. The $y+$ value oscillates between 1.2 for the tiny grid and 0.3 for the fine one for a Mach number of 0.85 with a lift coefficient of 0.5. These meshes are referred to in this paper as the DPW grids. More information about the generation of these meshes can be found in the article of Vassberg [14].

The second set of grids was generated by the IDEA Research Chair at Polytechnique Montréal.[***] This set consists of four structured meshes with an H-O topology, whereby each edge has been divided sequentially by 1.3/1.5/1.3 during the refinement sequence. The coarse, medium, fine, and extrafine grids have 3.0, 5.9, 22, and 51 million cells, respectively. The value of $y+$ oscillates from 0.31 to 0.12 for a Mach number of 0.85 with a lift coefficient of 0.5. A symmetric cut of the medium mesh is presented in Fig. 7. These meshes are referred as the IDEA grids.

For the second DPW-5 test case, the buffet study, a supplementary mesh was used. This mesh was generated by refining the IDEA medium grid at the wing from the root up to 33% of the wing span to better resolve flow separation occurring there. This mesh has 7.3 million cells.

All CFD computations have been performed with ANSYS-Fluent 13.0. A density-based solver has been used with a Roe Flux-Difference Splitting (Roe-FDS) scheme, implicit formulation, and with a second-order spatial discretization. Convergence has been accelerated by using multigrid algorithm with an F cycle. For the first test case, a refinement study, only the Spalart–Allmaras turbulence model (S–A) has been selected. For the second test case, which is the buffet study, both the Spalart–Allmaras and the k-ω shear stress transport (SST) turbulence model have been used. Turbulence boundary conditions have been imposed following guideline of the NASA turbulence modeling group.[†††] For each computation, the converged residuals were in the range of 10^{-5} to 10^{-9}, usually achieved within 1000 iterations. Typical convergence curves are showed in Fig. 8. Each run was started from freestream conditions to avoid the occurrence of hysteresis phenomena.

IV. Refinement Study

The first test case of DPW-5 is a refinement study for a fixed lift coefficient of 0.500 ± 0.001 with a Mach number of 0.85. The Reynolds number is 5×10^6, based on a reference chord of 275.80 in. The reference temperature is 100°F. For this study, both the DPW and IDEA sets of grids were used. Figure 9 presents the C_P curves at eight different stations and η ranging from 10 to 97% of the wing span. The black and red curves are the results computed on the medium DPW mesh and on the fine IDEA mesh, respectively. At station 1, the results computed on the DPW mesh indicate a small flow separation at the trailing edge. This separation, visible on Fig. 10, is not visible on the results computed on the IDEA mesh. Station 8 shows that the successive shock waves exhibit minor differences. The results agree well overall.

[§§]There are many configurations with a tail, but none of these was used at DPW-5.

[¶¶]Data available online at ftp://cmb24.larc.nasa.gov/outgoing/DPW5/unstructured_grids.REV01/ [retrieved 20 February 2012].

[***]Data available online at ftp://cmb24.larc.nasa.gov/outgoing/DPW5/contrib/POLY_IDEA_GRIDS/ [retrieved 15 May 2013].

[†††]Data available online at http://turbmodels.larc.nasa.gov/.

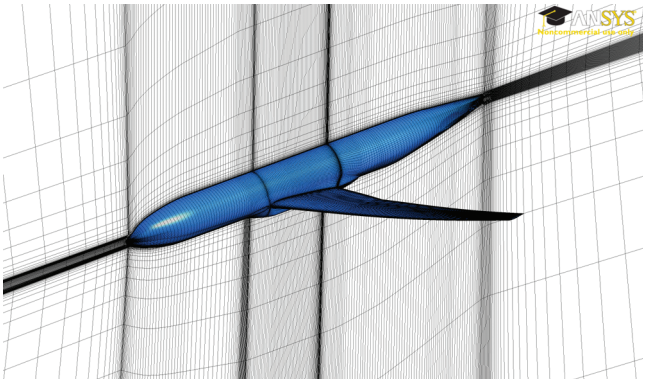

Fig. 7 Symmetric cut of the medium IDEA mesh (5.9 million cells).

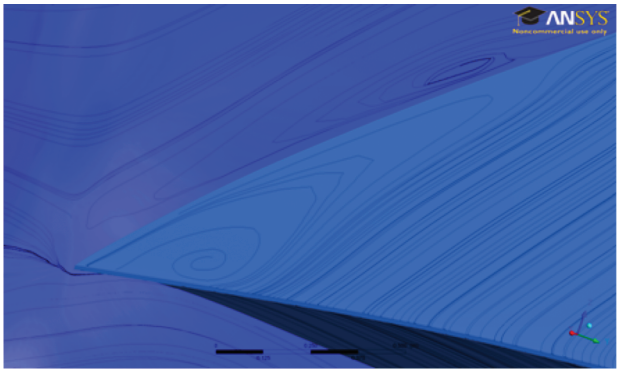

Fig. 10 Bubble separation on the DPW mesh at station 1.

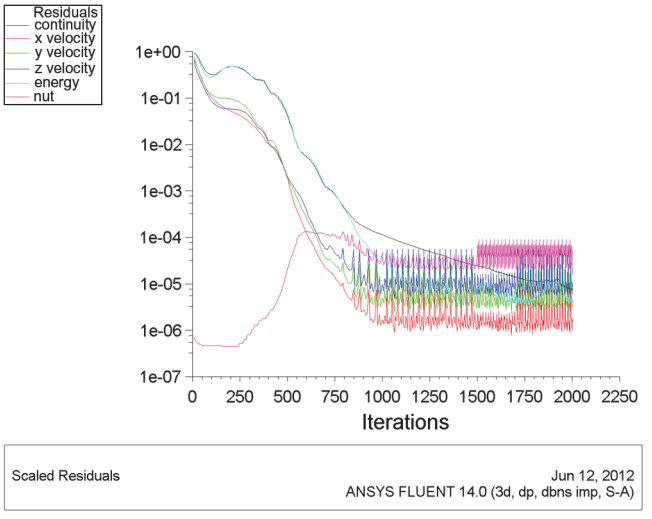

Fig. 8 Typical convergence curves.

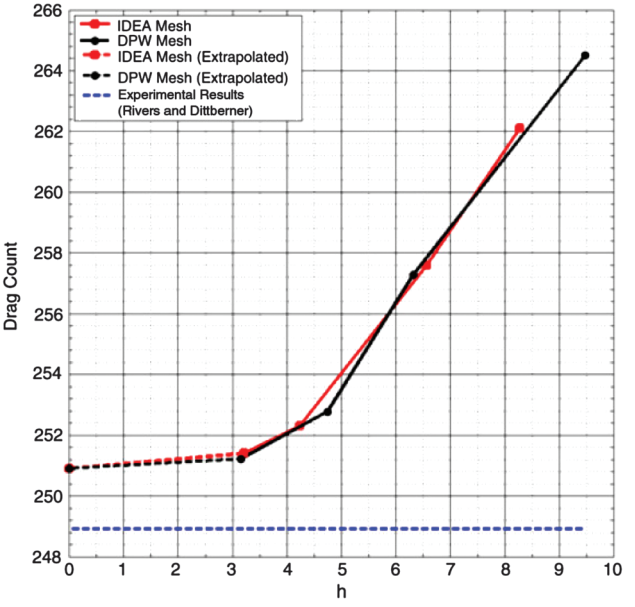

Fig. 11 Grid convergence study of far-field drag (case No. 1).

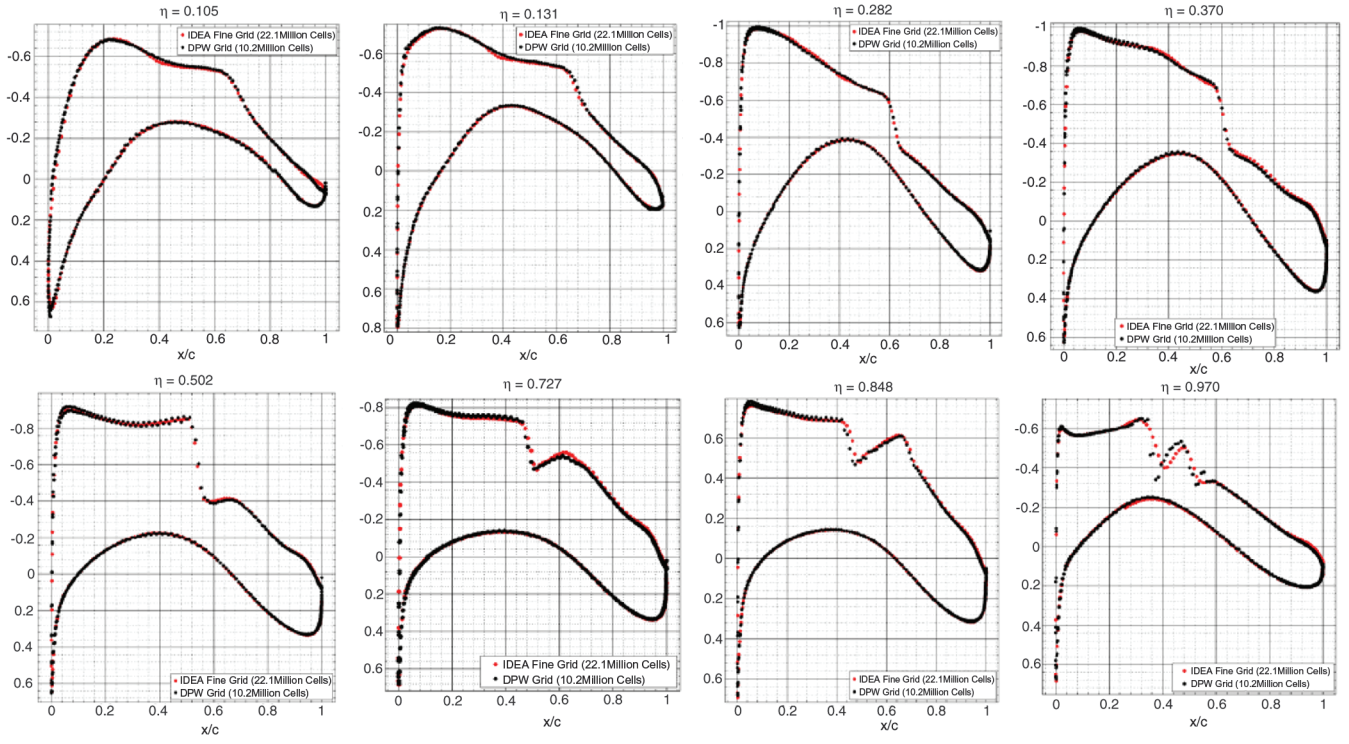

Fig. 9 Pressure coefficient curves on DPW and IDEA medium grids.

Figure 11 presents the grid convergence study of the far-field drag, computed with Eq. (14). The parameter h is computed as follows:

$$h = \left[\frac{1}{N}\sum_{i=1}^{N}(\Delta V_i)\right]^{1/3} \tag{17}$$

where N represents the number of cells of the computational domain and ΔV_i is the volume of the ith cell. The black and red curves are the results computed on the DPW and IDEA grids. The dashed line indicates extrapolated values computed following the guidelines of Celik et al. [15]. The blue line represents the experimental drag coefficient value of Rivers and Dittberner [16].

The apparent order computed [15], p, is 3.5 for the IDEA set of grids and 4.2 for the DPW one. The extrapolated values are identical for both sets of grids, giving a value of 250.9 drag counts. This agrees with the experimental value of 248.9 within two counts. The two curves exhibit the same behavior and are almost superimposed, showing that the flow solution is nearly mesh independent, considering the major differences in mesh topologies.

Figure 12 shows the drag convergence curves, again for the far-field drag, i.e., Eq. (14), but also for the net drag, i.e., Eq. (15). Recall that the net drag is the far-field drag in which the spurious drag has been removed. The solid and dashed red curves represent the far-field and net drag computed on the IDEA meshes, respectively, whereas the solid and dashed black curves represent the far-field and net drag computed on the DPW meshes, respectively. The dashed blue line represents the experimental value of Rivers and Dittberner [16]. The two net drag curves show the same behavior and are almost superimposed. Also, the two curves exhibit almost no variation (less than 0.1 drag count) for an h value smaller than or equal to four. Figures 11 and 12 show that, even when h tends toward zero, there is some residual spurious drag that cannot be removed by refining the mesh. Indeed, the extrapolated value of the far-field drag is 250.9 drag counts, whereas the converged value of the net drag is 248.8 for the DPW meshes and 249.1 for the IDEA meshes. This figure shows the strength of the far-field drag decomposition method: it allows increased accuracy on coarser meshes when spurious drag is extracted, in many cases achieving better results than computations on finer meshes without spurious drag removal.

Figure 13 shows the convergence curves of the viscous, wave, induced, and spurious drag computed on the IDEA meshes with Eqs. (7), (8), (10), and (9), respectively. The red dashed curve represents the theoretical value of the induced drag computed with the theoretical formula $Cd_i = C_L^2/\pi\lambda$. This value was computed with an Oswald factor of 1, which is not representative of the actual Oswald factor of the CRM wing, that factor being estimated at between 0.92 and 0.97. The figure shows that induced drag is slightly affected by grid refinement. This is explained by the fact that induced drag is generated by a reversible phenomenon. The same behavior can be observed for the wave drag, which is also nearly independent

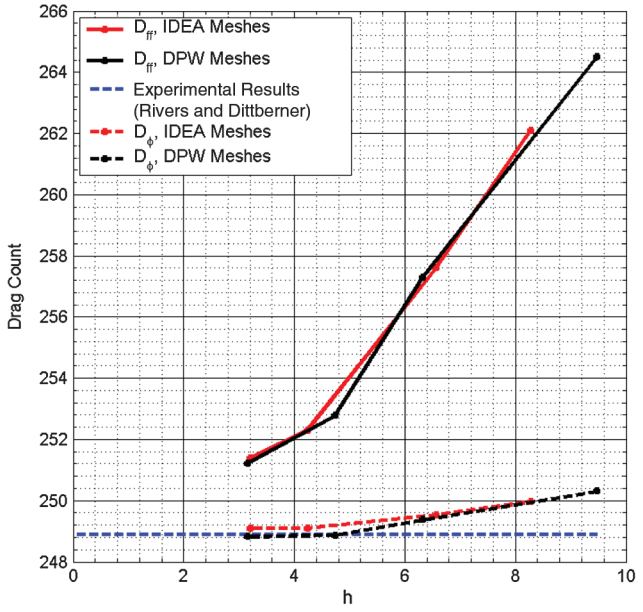

Fig. 12 Grid convergence study of net and far-field drag (case No. 1).

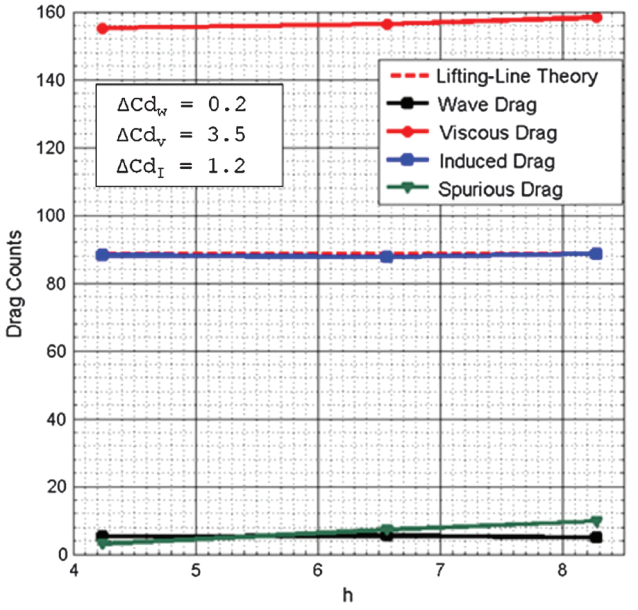

Fig. 13 Grid convergence study of the physical components of drag (case No. 1).

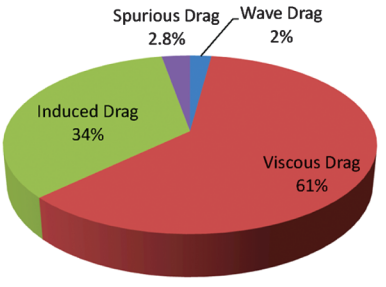

	Wave	Viscous	Induced	Spurious	Total
Drag Count	5.5	156.0	87.7	7.3	249.2

Fig. 14 Physical drag decomposition (case No. 1).

of the mesh refinement. However, viscous drag displays strong dependence on mesh refinement. Finally, there is agreement between the theoretical and computed values of induced drag.

Figure 14 shows the physical drag decomposition for the results computed on the IDEA medium mesh (5.9 million cells). Viscous drag accounts for 61% of the total drag, induced drag for 34%, and wave drag for 2%, which is less than the spurious drag. This drag decomposition shows the advantage of the far-field method for an aerodynamics engineer running an optimization process aimed at reducing the net drag. In fact, the decomposition indicates that induced drag reduction is a more likely candidate for redesign than wave drag reduction because the latter is already near optimal.

V. Buffet Study

The second test case is a buffet study with a fixed Mach number of 0.85, in which the angle of attack varies from 2.5 to 4.0 deg. The objective of this study is to predict the buffet conditions. Buffet onset starts when the slope of the curve C_L vs C_M changes sign. In accordance with the general guidelines of DPW-5, this analysis

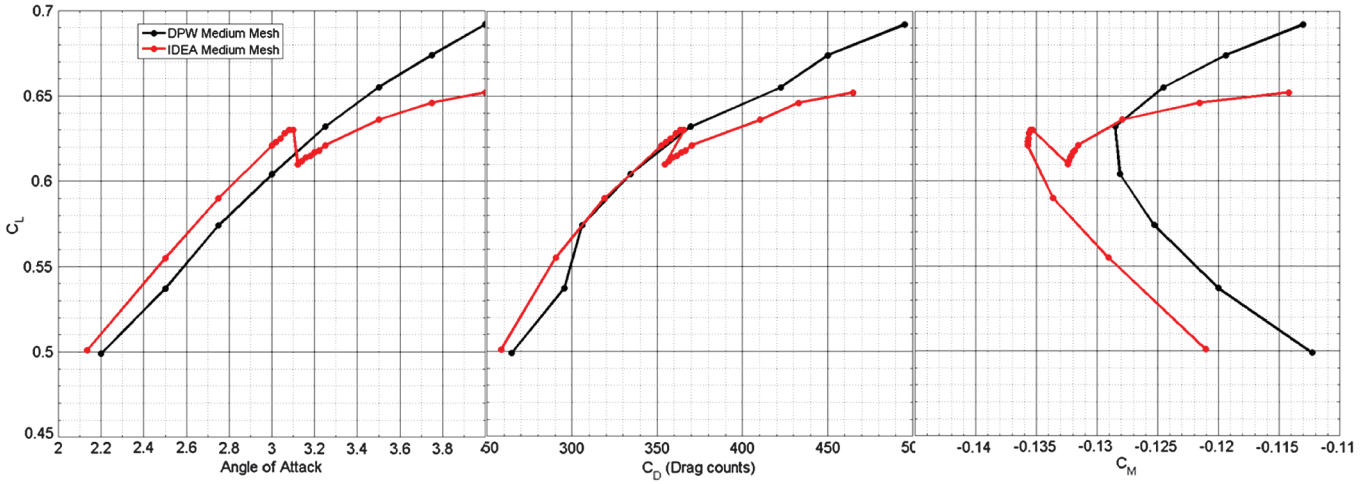

Fig. 15 C_L vs α, C_L vs C_D, and C_L vs C_M curves.

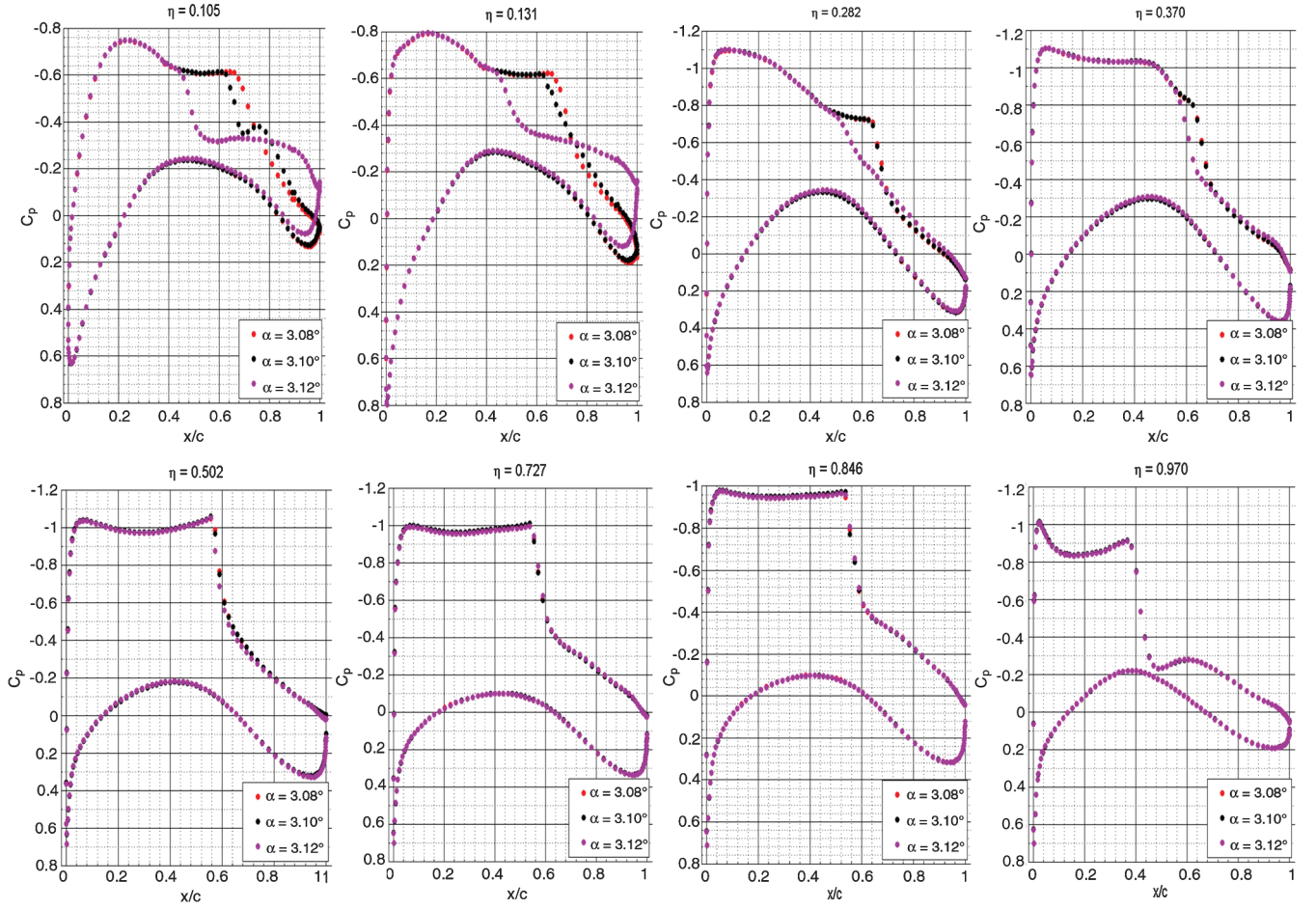

Fig. 16 C_p curves at eight different stations for three different angles of attack.

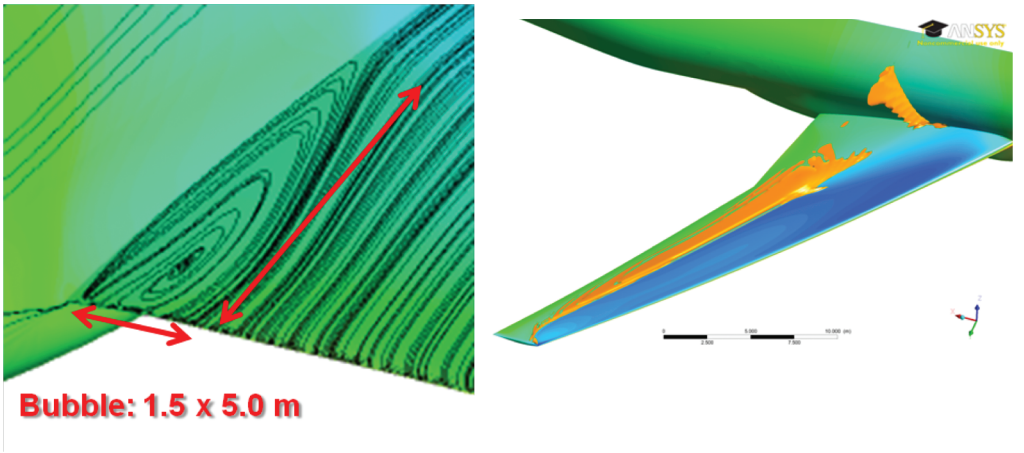

Fig. 17 Streamlines and shock wave detected with Eq. (11) for an angle of attack of 3.12 deg.

should be performed on a medium mesh, either custom or provided by the DPW-5 committee. For the first part of this study, both the DPW and IDEA meshes were used.

Figure 15 shows the C_L vs α, C_L vs C_D, and C_L vs C_M curves using results computed with the S–A turbulence model on the DPW medium mesh (black curves) and on the IDEA medium mesh (red curves). Analysis of this figure shows that the C_L vs C_M curve changes slope at $C_L = 0.63$ for both meshes, corresponding to angles of attack of 3.12 and 3.25 deg for the IDEA and DPW meshes, respectively. According to the lift coefficient-moment coefficient (CL-CM) slope buffet criterion, this would signal buffet onset. On the IDEA curves, a C_L break can be observed at the buffet onset associated with a loss of drag. This C_L break is not visible on the DPW curve. According to Roskam and Lan [17], this behavior is evidence of buffet onset. Figure 16 shows the C_p curves for 3.08, 3.10, and 3.12 deg angles of attack computed on the IDEA mesh at eight different wing stations. The figure indicates major flow separation at the wing root for an angle of attack of 3.12 deg. This separation starts from the root and extends to around 17% of the wing span. A separation bubble is visible in the streamline patterns shown in Fig. 17, which also shows the shock wave detected with Eq. (11). The picture on the right-hand side of Fig. 17 shows a loss of around 17% of the shock wave for an angle of attack of 3.12 deg, according to the C_p curves presented in Fig. 16.

To understand the physical consequences of the drag loss associated with the lift loss, far-field drag visualization has been done. Results are shown in Fig. 18. The red, blue, and black solid lines represent total, wave, and viscous drag, respectively. The dashed red and black lines represent the induced and spurious drag. Finally, the black circle represents the theoretical induced drag predicted by the lifting line theory. Globally, lift decreases by 3.2% (this loss can be observed in Fig. 15) and total drag by 2.8%. The flow separation induces a major change in the spanwise loading of the wing between 3.10 and 3.12 deg, which decreases the wave drag by 23.1% and the induced drag by 6.5%, whereas increasing the viscous drag by 4.1%. According to the theory of Roskam and Lan [17], this sudden change in the load of the wing can be considered as an indication of buffet onset.

The flow separation analyzed in the preceding section does not appear in results computed on the DPW mesh. Furthermore, the DPW-5 summary [18] records that some participants found this C_L break, whereas others did not. To analyze the possible causes of the presence or absence of the C_L break, two aspects are analyzed here: the turbulence model and the level of mesh refinement.

A. Turbulence Model Analysis

Because turbulence models have different response levels in the presence of adverse pressure gradient flow separation, additional CFD simulations were conducted on the DPW and IDEA medium meshes with the Spalart–Allmaras and the k-ω SST turbulence models. Figure 19 shows the resulting C_L vs α and C_L vs C_D curves. The black and red lines represent the results computed with the DPW and IDEA meshes, respectively. Solid and dashed lines indicate the results computed with the Spalart–Allmaras and k-ω SST model, respectively. For all the results, the lift computed with the k-ω SST model at a given angle of attack is less than the lift computed with the S–A model. The results computed on the IDEA mesh show a lift and drag break for both turbulence models, the break occurring at $C_L = 0.62$ for the S–A turbulence model and at $C_L = 0.605$ for the k-ω SST model. No lift break is visible for either turbulence model when results are computed on the DPW mesh.

From these results, it is possible to infer that the turbulence model played no role in the observed C_L break.

B. Refinement Analysis

Mesh refinement plays an important role in capturing boundary-layer separation. The objective is to demonstrate that the absence of a C_L break on the results computed on the DPW mesh is caused by insufficient refinement at the wing root. One way to do so would be to perform buffet studies on the DPW fine mesh and determine whether or not boundary-layer separation occurs at the wing root. However, convergence could not be achieved on the fine mesh at critical angles of attack, and this mesh could not be modified because it had been supplied by the DPW committee. Instead, a mesh refinement study was performed with the IDEA coarse and medium meshes. A third mesh was generated from the medium mesh, containing a refinement

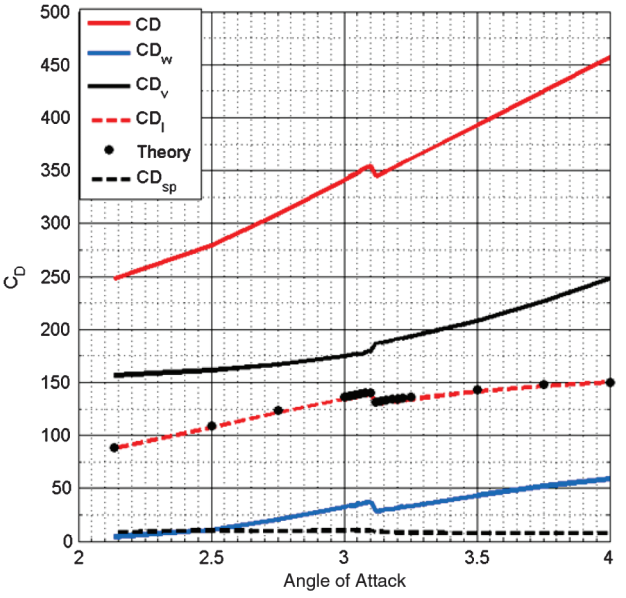

Fig. 18 Far-field drag decomposition method applied to the results computed on the IDEA mesh.

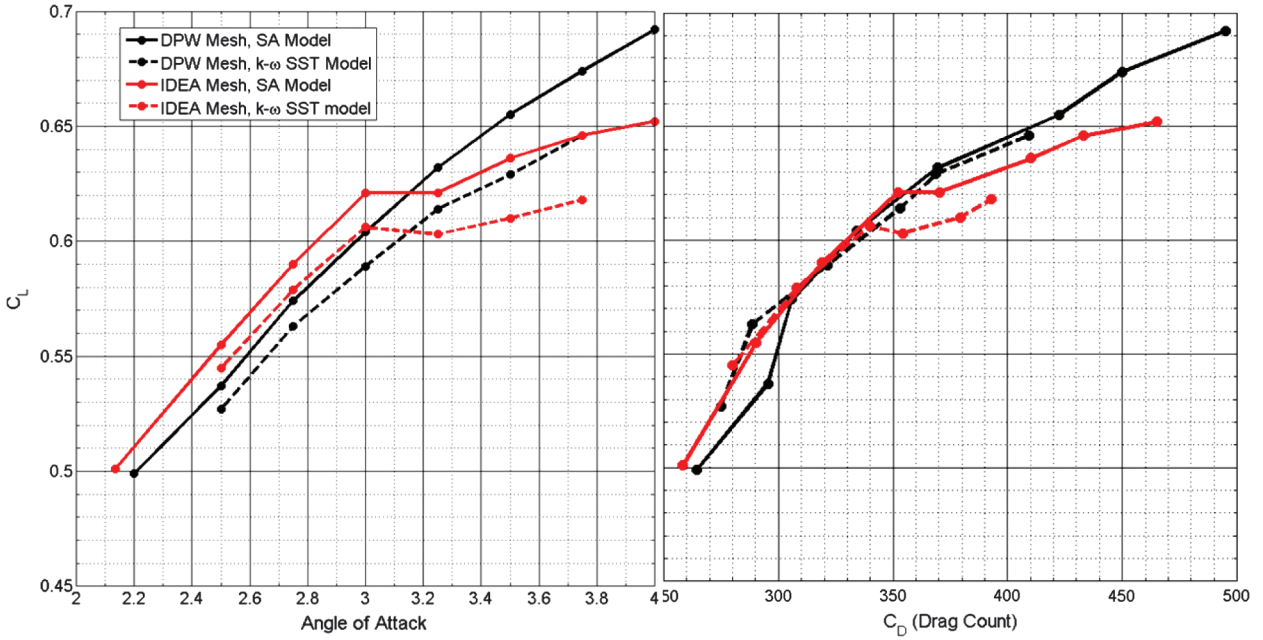

Fig. 19 Investigation of the turbulence model effect.

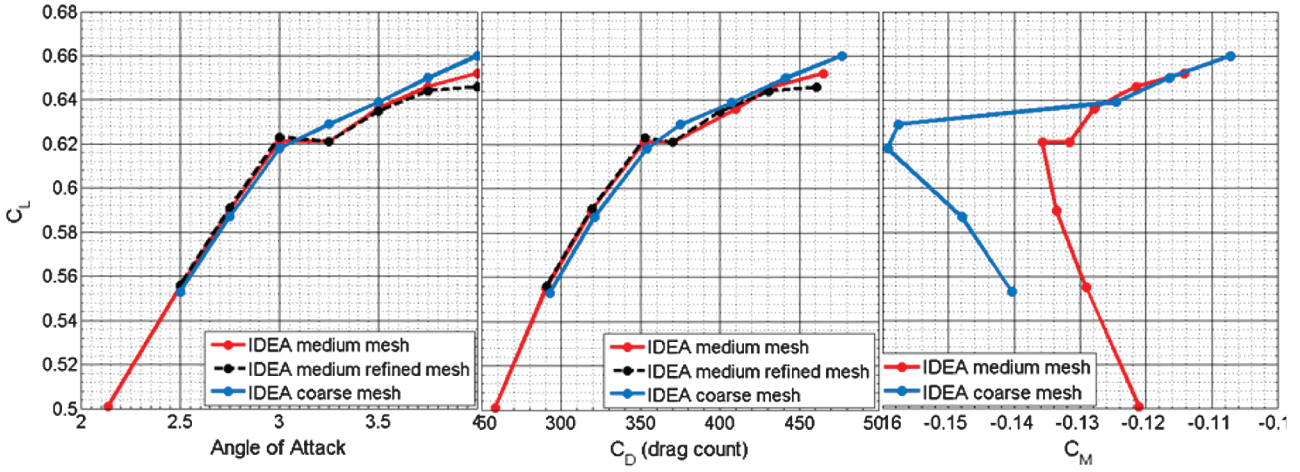

Fig. 20 Investigation of the mesh refinement.

at the wing root, where flow separation occurs. This refinement at the root was accomplished by dividing each edge in the vicinity of the flow separation by a factor of 2. The new mesh has 7.3 million cells, compared to 5.9 million for the original medium IDEA mesh. Figure 20 shows the C_L vs α, C_L vs C_D, and C_L vs C_M curves computed with these three meshes: the solid red line for the medium mesh, the black dashed line for the refined medium mesh, and the blue solid line for the coarse mesh. The analysis of this figure clearly shows that there is no lift loss on the coarse mesh, but there is one on both the medium and refined medium meshes. Further analysis of the CFD solutions also shows that there is no flow separation on the coarse mesh, whereas there is one on both the medium and refined medium meshes. Finally, there is neither drag loss nor shock wave separation on the coarse mesh. Analysis of the C_L vs C_M curve indicates the change in slope on both the IDEA coarse and medium mesh occurring at around $C_L = 0.62$. According to the CL-CM slope criterion, this change coincides with buffet onset. Finally, a comparison of the curves in Figs. 15 and 20 shows that the curves computed on the IDEA coarse mesh have the same properties as those computed on the DPW medium mesh.

C. Far-Field Analysis

The far-field drag decomposition method was used to extract the spurious drag from the results of the buffet study. Figure 21 shows the

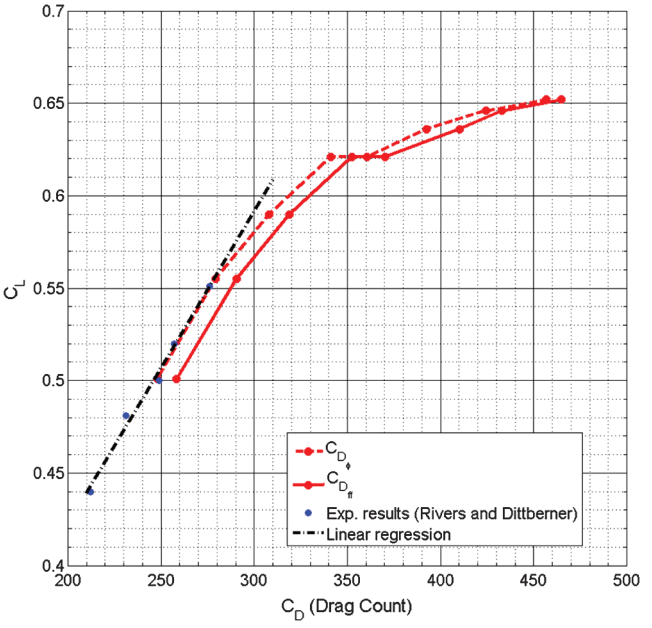

Fig. 21 Far-field method applied to the buffet study.

C_L vs C_D curves generated from the results computed on the IDEA medium mesh. The red solid line represents the C_L vs C_D, in which the far-field drag is computed with Eq. (14), whereas the red dashed line represents the net drag computed with Eq. (15). The blue circles represent the experimental data of Rivers and Dittberner [16]. The dashed black line represents the linear regression of the experimental data. The net drag agrees with the available experimental results, showing that accurate results can be obtained on coarse and medium meshes by the far-field method.

VI. Conclusions

Two test cases of the Drag Prediction Workshop (DPW) 5 series have been analyzed with the previously developed and modified far-field drag decomposition method. This method has two principal advantages. First, it allows extraction of the spurious drag that is caused by numerical and truncation errors. Second, it allows decomposition of the drag into its physical components: viscous drag, induced drag, and wave drag. The Drag Prediction Workshop series is dedicated to assessing the state of the art in numerical methods used as tools to predict aerodynamic coefficients. The two test cases studied here involved grid convergence and buffet onset prediction.

The grid convergence study was conducted at a fixed Mach number of 0.85 and a lift coefficient of 0.5, which correspond to the design cruise conditions. Two sets of grids were used. The first was supplied by the DPW committee and the second was generated by the IDEA Research Chair team. The two sets of grids are based on different topologies. The DPW grids have an O-O topology, and the IDEA grids have an H-O topology. The results show comparable accuracy on the two grids. Furthermore, they show that net drag, which is the total drag after spurious drag removal, computed on a coarse mesh is closer to the experimental value than total drag computed on finer meshes.

The buffet study was conducted at a fixed Mach number of 0.85, in which the angle of attack ranged between 2.5 and 4.0 deg. The results computed on the DPW and IDEA medium meshes showed a major difference between the C_L vs α curves for these grids: the IDEA grids showed a lift loss at a 3.12 deg of angle of attack, whereas the DPW grid results did not. An investigation was carried out using the far-field method to understand the reason for this difference. It was shown that the lift loss obtained on the IDEA grid is caused by flow separation occurring at the root of the wing at buffet onset. The associated drag loss is mainly caused by the decrease in wave drag stemming from the loss of 25% of the shock wave strength on the wing as well as by the reduction of induced drag via lift reduction. This loss causes a change in the spanwise wing loading. Investigation was also conducted to understand why the DPW grid does not exhibit this lift and drag loss. It concludes that mesh refinement plays a critical role in capturing wing root flow separation. Furthermore, buffet onset can be detected by the departure of the lift coefficient from linearity when analyzing a C_L vs α curve or by a sudden change in the axial force. The computational fluid dynamics solution obtained on the IDEA grid had these properties. Finally, the far-field drag decomposition method was applied to the C_L vs C_D curve, in order to extract the spurious drag. Again, the results show strong agreement with the available experimental results for low angles of attack, even on relatively coarse meshes.

Acknowledgments

This research was conducted by the IDEA Industrial Research Chair, which is supported by the Natural Sciences and Engineering Research Council of Canada, the Joseph-Armand Bombardier Foundation, and Pratt and Whitney Canada. The authors thank Eddy Petro and Quentin Lux, both members of the IDEA Chair, for their important contribution to the meshing and CFD simulations. They also thank the Reseau Québécois de Calcul de Haute Performance (RQCHP) and Compute Canada, particularly Richard Lefebvre and Michel Béland, for their support.

References

[1] van Dam, C., "Aircraft Design and the Importance of Drag Prediction," *CFD-Based Aircraft Drag Prediction and Reduction*, Vol. 2, von Karman Institute for Fluid Dynamics, Rhode-St-Genèse, Belgium, 2003, pp. 1–37.

[2] Meredith, P., "Viscous Phenomena Affecting High-Lift Systems and Suggestions for Future CFD Development," AGARD TR-94-18415-04-01, Sept. 1993.

[3] Van der Vooren, J., and Destarac, D., "Drag/Thrust Analysis of Jet-Propelled Transonic Transport Aircraft: Definition of Physical Drag Components," *Aerospace Science and Technology*, Vol. 8, No. 7, 2004, pp. 545–556. doi:10.1016/j.ast.2004.09.001

[4] Van der Vooren, J., and Slooff, J., "CFD-Based Drag Prediction: State-of-the-Art, Theory, Prospects," National Aerospace Lab. TR-TP90247, The Netherlands, 1990.

[5] Gariépy, M., Trépanier, J.-Y., and Masson, C., "Convergence Criterion for a Far-Field Drag Prediction and Decomposition Method," *AIAA Journal*, Vol. 49, No. 12, 2011, pp. 2814–2818. doi:10.2514/1.J050865

[6] Laurendeau, E., and Boudreau, J., "Drag Prediction Using the Euler/Navier-Stokes Code FANSC," *SAE Transactions*, Vol. 112, No. 1, 2003, pp. 488–499. doi:10.4271/2003-01-3022

[7] Gariépy, M., and Trépanier, J., "A New Axial Velocity Defect Formulation for a Far-Field Drag Decomposition Method," *Canadian Aeronautics and Space Journal*, Vol. 58, No. 02, 2012, pp. 69–82. doi:10.5589/q12-006

[8] Méheut, M., and Bailly, D., "Drag Prediction and Wake Survey Techniques," *CEAS Katnet Conference on Key Aerodynamic Technologies*, Paper TP2005-102, 2005.

[9] Méheut, M., and Bailly, D., "Drag Breakdown Methods from Wake Measurements," *AIAA Journal*, Vol. 46, No. 4, 2008, pp. 847–862. doi:10.2514/1.29051

[10] Esquieu, S., "Évaluation de la Traînée d'un Avion de Transport á Partir de Calculs Numériques de Mécanique des Fluides," Ph.D. Dissertation, Mécanique, Université Bordeaux 1, 2003.

[11] Lovely, D., and Haimes, R., "Shock Detection from Computational Fluid Dynamics Results," AIAA Paper 1999-3285, 1999, pp. 1–9.

[12] Tognaccini, R., "Methods for Drag Decomposition, Thrust-Drag Bookkeeping from CFD Calculations," *CFD-Based Aircraft Drag Prediction and Reduction*, Vol. 2, von Karman Institute for Fluid Dynamics, Rhode-St-Genèse, Belgium, 2003, pp. 1–65.

[13] Vassberg, J., DeHaan, M., Rivers, M., and Wahls, R., "Development of a Common Research Model for Applied CFD Validation Studies," AIAA Paper 2008-6919, 2008.

[14] Vassberg, J., "A Unified Baseline Grid About the Common Research Model Wing-Body for the Fifth AIAA CFD Drag Prediction Workshop," AIAA Paper 2011-3508, June 2011.

[15] Celik, I., Ghia, U., Roache, P., Freitas, C., Coleman, H., and Raad, P., "Procedure for Estimation and Reporting of Uncertainty Due to Discretization in CFD Applications," *Journal of Fluids Engineering*, Vol. 130, No. 7, 2008, pp. 078001-1–078001-4. doi:10.1115/1.2960953

[16] Rivers, S., and Dittberner, A., "Experimental Investigations of the NASA Common Research Model in the NASA Langley National Transonic Facility and NASA Ames 11-Ft Transonic Wind Tunnel (Invited)," *49th AIAA Aerospace Sciences Meeting*, AIAA Paper 2011-1126, Jan. 2011.

[17] Roskam, J., and Lan, C.-T. E. L., *Design, Analysis and Research Corporation (DARCorporation)*, Lawrence, Kansas, USA, 2003, pp. 585–600.

[18] Levy, David W., Laflin, Kelly R., Tinoco, Edward N., Vassberg, John C., Mani, Mori, Rider, Ben, Rumsey, Chris, Wahls, Richard A., Morrison, Joseph H., Brodersen, Olaf P., Crippa, Simone, Mavriplis, Dimitri J., and Murayama, Mitsuhiro, "*Summary of Data from the Fifth AIAA CFD Drag Prediction Workshop*," AIAA Paper 2013-0046, Jan. 2013, pp. 1–31.